Quaternary Science Reviews 218 (2019) 254–266

Contents lists available at ScienceDirect

Quaternary Science Reviews

journal homepage: www.elsevier.com/locate/quascirev

# A Late Glacial surface rupturing earthquake at the Peel Boundary fault zone, Roer Valley Rift System, the Netherlands

R.T. Van Balen [a, b, *], M.A.J. Bakker [b], C. Kasse [a], J. Wallinga [c], H.A.G. Woolderink [a]

[a] Department of Earth Sciences, VU University Amsterdam, De Boelelaan 1085, 1081 HV, Amsterdam, the Netherlands
[b] TNO - Geological Survey of the Netherlands, Princetonlaan 6, 3584 CB, Utrecht, the Netherlands
[c] Netherlands Centre for Luminescence Dating & Soil Geography and Landscape Group, Wageningen University & Research, Droevendaalsesteeg 3, 6708 PB, Wageningen, the Netherlands

ARTICLE INFO

*Article history:*
Received 28 March 2019
Received in revised form
21 June 2019
Accepted 27 June 2019

*Keywords:*
Earthquake
Glacio-isostacy
Trench
Rupture length

ABSTRACT

Paleoseismological trenching studies constrain recurrence times and magnitudes of faulting events and earthquakes on active faults. In a trench along the central part of the Peel Boundary fault zone (PBFZ), southeastern Netherlands, evidence was found for such a large faulting event that occurred around 14 ka. The event caused a fault scarp in unconsolidated sediments of ~1 m height. A colluvial wedge was formed next to the scarp. A second faulting event offsets this colluvial wedge by 0.2–0.1 m. This event can be tentatively dated at ~13 ka. During or immediately after the second event, a large clastic dyke intruded along the fault plane. The dyke is not faulted, but its emplacement did cause some minor thrust faulting around the injection.

The sudden character of the main faulting event, the brittle deformation style of loam layers, the lack of growth faulting in the colluvial wedge, the clastic dykes and the flame structures demonstrate that the main faulting event was a surface rupturing earthquake. Based on the scarp height, the estimated moment magnitude is about $6.8 \pm 0.3$. Similar observations in a previous trench site suggest that the length of the surface rupture was at least 32 km. The earthquake took place during the Weichselian (Würmian) Late Glacial. This timing corresponds to the start of the glacio-isostatic forebulge collapse in the Netherlands. Glacio-isostatic movements have been invoked before to explain earthquake events in the Roer Valley Rift System in which the PBFZ is situated, and in northern Germany and Denmark. If these earthquakes can indeed be attributed to a collapsing forebulge, their ages should show a decrease in the direction of ice-sheet retreat. This might indeed be the case, as the ages decrease from 14 ka and 13 ka in this trench via 13–16 ka at the Osning Thrust Zone, NW Germany, to 12–14 ka in northern Denmark.



## 1. Introduction

The Roer Valley Rift System (RVRS; Fig. 1) is an active rift system situated in the southern part of the Netherlands and adjoining areas in Belgium and Germany (Fig. 1; Geluk et al., 1994; Van Balen et al., 2005). The RVRS is situated in the northwestern part of the European Cenozoic Rift System (Ziegler, 1992; Michon et al., 2003). The last extension phase started at the Oligocene-Miocene transition (Ziegler, 1992; Michon et al., 2003) and is still ongoing (Michon and Van Balen, 2005; Van Balen et al., 2005). The RVRS is characterized as a slow deforming area with occasional earthquakes (e.g. Camelbeeck et al., 2007; Caro Cuenca et al., 2013; Grützner et al., 2016; Kübler et al., 2017). The Roer Valley Graben (RVG) is located in the central part of the RVRS. It is bounded by the Feldbiss Fault zone (FFZ) in the southwest and the Peel Boundary Fault zone (PBFZ) in the northeast (Fig. 2b). These two fault zones and the continuation of the PBFZ into Germany (i.e. the Erft- and Rurrand faults), are at present the seismically most active faults in the rift system (Camelbeeck et al., 2007). The last moderate earthquake in the RVRS was the Roermond earthquake of 1992 (Ml 5.8; Ms 5.4). It probably took place along one of the faults of the PBFZ (Van Eck and Davenport, 1994), and was accompanied by fissure eruptions of liquefied sand, landsliding in sandpits, and minor damage to houses and infrastructure. The return period for this size earthquake in the RVRS is around 260 years (Camelbeeck et al., 2007). Like all other historic earthquakes in the RVRS (Grützner et al., 2016), there was

* Corresponding author. Department of Earth Sciences, VU University Amsterdam, De Boelelaan 1085, 1081 HV, Amsterdam, the Netherlands.
*E-mail address:* r.t.van.balen@vu.nl (R.T. Van Balen).

https://doi.org/10.1016/j.quascirev.2019.06.033
0277-3791/

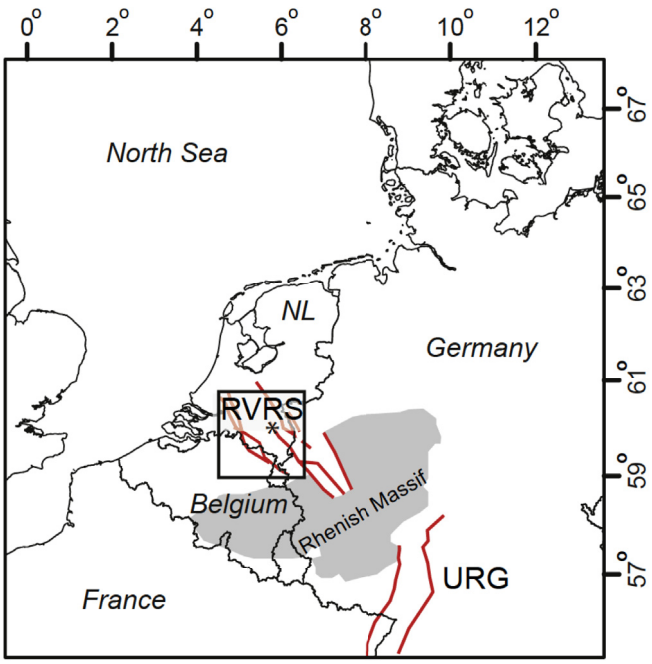


**Fig. 1.** Location of the study area in Northwestern Europe. RVRS = Roer Valley Rift System, URG = Upper Rhine Graben. Coordinate system is in lat-lon using UTM projection. The asterisk indicates the location of the studied fault trench near Bakel.

no surface rupture during the Roermond earthquake.

The 1992 earthquake was the incentive for renewed scientific research into the activity of faults in the RVRS and adjoining parts of the Lower Rhine Embayment (LRE), using trenches. In a synthesis of the results of six of those trenches, Houtgast et al. (2005) concluded that most of the reconstructed faulting events have taken place during the Late Glacial period, roughly from 10 to 15 ka. Because of the timing, they speculated on a causal relationship between faulting and glacio-isostatic motions in response to the Weichselian deglaciation. However, also a few older and younger displacement events have been inferred in trench studies (e.g. Camelbeeck et al., 2007; Vandenberghe et al., 2009; Grützner et al., 2016; Vanneste et al., 2018).

In the fall of 2014 a trench was opened across one of the faults of the PBFZ, near the town of Bakel (Figs. 1 and 2). The trenching was part of a broad project in which public awareness of the existence of the faults, their importance for the environment (e.g. via groundwater management and spatial planning) was leading. The fault trench attracted many visitors and gained large media attention. This paper documents the scientific observations and presents a reconstructed sequence of events. Finally, we re-address the long lasting and non-conclusive debate about the seismic-versus creep nature of near surface fault displacements in the RVRS (Ahorner, 1962; Houtgast et al., 2003, 2005; Demoulin, 2006; Camelbeeck et al., 2007; Grützner et al., 2016; Kübler et al., 2017; Verbeeck et al., 2017).

## 2. Setting

### 2.1. Tectonic setting

The trench site is located on the Peel Boundary Fault zone (PBFZ), the roughly NW-SE oriented northeastern boundary fault of the RVG. The PBFZ is a Mesozoic, or possibly Paleozoic, fault structure, which has been reactivated several times in normal and reverse faulting modes (Geluk et al., 1994). The last and still ongoing normal faulting phase started during the Late Oligocene (Ziegler, 1992; Michon et al., 2003; Michon and Van Balen, 2005; Van Balen et al., 2005). At the surface the PBFZ is characterized by fault scarps. The scarps have varying heights, as a result of laterally variable displacement rates and smoothing due to erosion and/or blanketing by young deposits. At locations without erosion or blanketing, the scarps are up to several meters high in the northwestern part of the fault zone and about one meter high in the southeastern part. The faults of the PBFZ offset geomorphic markers, like Pleniglacial and Late Glacial fluvial terraces and Younger Dryas dunes along the Meuse river (Van den Berg et al., 2002; Houtgast et al., 2002; Michon and Van Balen, 2005; Woolderink et al., 2018). The inferred displacement style is pure normal faulting, despite the slightly oblique extension of the rift system (Michon et al., 2003). DEM analyses, aerial photographs and borehole data show that near the surface the PBFZ consists of a large number of en echelon faults, with orientations ranging from NNW-SSE to NW-SE (Van den Berg et al., 2002; Michon and Van Balen, 2005; Van Balen et al., 2005). The trench site was located across one of the faults in the central part of the PBFZ, at a step-over link between two fault segments (Fig. 2).

### 2.2. General stratigraphy of the shallow subsurface

In the trench area the shallow deposits of the RVRS consist of coarse-grained fluvial deposits formed by the Meuse river, grouped into the Beegden Formation (Fig. 3). These deposits are overlain by fine-grained sand and loam deposits, formed by local fluvial, aeolian and lacustrine processes. These latter deposits are part of the Boxtel Formation (Schokker et al., 2007). Being the youngest depositional sequence at the study site, the litho- and chronostratigraphy of the upper part of the Boxtel Formation is very important for determining the fault displacement history in the trench. The uppermost part of the Boxtel Formation corresponds to the Weichselian coversand series (e.g. Kasse et al., 2007; Vandenberghe et al., 2013), which occur widespread in large parts of NW and Central Europe. The coversand series are subdivided into four main units. Sediments of the two lower units, the Older Coversand I and II units, generally consist of well-sorted, fine, silty sands. Their dominantly horizontal laminations reflect deposition as (extensive) aeolian sand sheets. The lower, Older Coversand I unit is strongly disturbed by syn- and postdepositional periglacial deformations, ranging from small-scale loading structures to large-scale involutions. The Older Coversand II unit is usually not cryoturbated. These two Older Coversand units are separated by an erosional unconformity and desert pavement of Late Pleniglacial age, the Beuningen Gravel Bed complex (BGB) (Vandenberghe et al., 2013, and references therein). Formation of the BGB complex was completed with a deflation phase lasting from ~16 to 14 ka.

Compared to the two Older Coversand units, the overlying two Younger Coversand units generally contain less silt, have a larger grain size and show horizontal to low-angle cross bedding, indicating aeolian deposition on dry flat surfaces and in the form of low dunes. However, sometimes the Older and Younger Coversand deposits appear similar, and the Lower Loamy Bed (Bølling, ~14.7–14.0 ka) which separates the two is not encountered. In such cases the deposits overlying the BGB cannot be separated into an Older Coversand II and Younger Coversand I unit (Kasse et al., 2018). In between the Younger Coversand I and II units a Late Glacial paleosol occurs, the Usselo Soil of Allerød and early Younger Dryas age. The soil is typically 5–30 cm thick, and it is frequently characterized by pieces of charcoal and mottling due to bioturbation/burrowing by dung beetles (e.g. Van Hoesel et al., 2012; Vandenberghe et al., 2013). Its age interval is estimated at circa

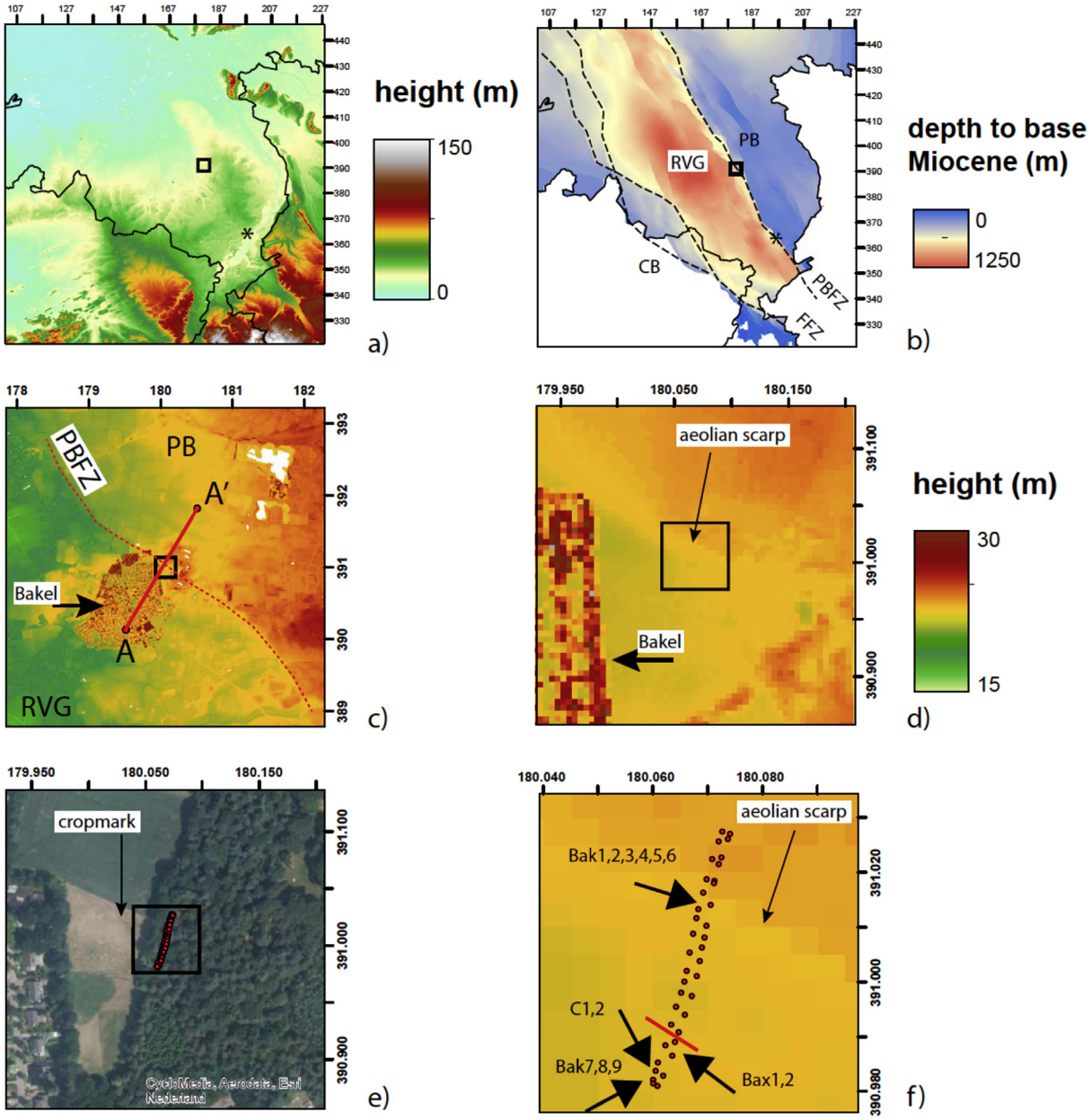


**Fig. 2.** Location and overview figures. Coordinate system is the Dutch National Grid (RD). PBFZ = Peel Boundary Fault Zone, FFZ = Feldbiss Fault Zone, RVG = Roer Valley Graben, CB = Campine Block, PB = Peel Block. a) Digital elevation model showing the topography of the Roer Valley Rift System and location of the study area. The * denotes the location of the Neer trench. The position of a) is indicated in Fig. 1 b) Depth to the base of the Miocene deposits, reflecting the differential neotectonic vertical motions in the rift system. c) Digital elevation model showing the topography around the study area near the village of Bakel. The fault trace is indicated by a dashed line. The straight red line (A-A′) indicates the position of the profile shown in Fig. 3. The position of c) is indicated in a) and b). d) Detail of the digital elevation model showing the area surrounding the fault trench. The terrain step within the rectangle is an expression of Medieval drift sand deposition, and does not correspond to the location of the fault (red line in f)). The position of d) is indicated in c). e) Aerial photograph of the same area as d). The trench (outlined by red dots) was located at the rim of a forested area, to ensure minimal anthropogenic disturbance. On the aerial photo the fault can be traced using crop and field marks. f) Close-up of the digital elevation model around the trench, showing the outline of the trench (red dots), the fault (red line), and the locations of the OSL and $^{14}C$ samples. The position of f) is indicated in e). . (For interpretation of the references to color in this figure legend, the reader is referred to the Web version of this article.)

13.9–12.85 ka (Hoek, 2001; Van Hoesel et al., 2012; Vandenberghe et al., 2013). The sediments of the overlying Younger Coversand II are of Younger Dryas age (12.85–11.7 ka). After aeolian deposition ceased, at approximately the Late Glacial – Holocene transition, Holocene soil formation took place. However, usually this soil formation was interrupted by several phases of drift-sand deposition (Sevink et al., 2013; Kasse et al., 2018). The most important drift-sand phase started during the Middle Ages.

## 3. Methods

### 3.1. Site selection and preparation

The position of the Peel Boundary fault Zone can often, but not always, be deduced from DEM data showing straight to arcuate terrain steps extending over several kilometers (Michon and Van Balen, 2005; Van Balen et al., 2005). These segments are usually

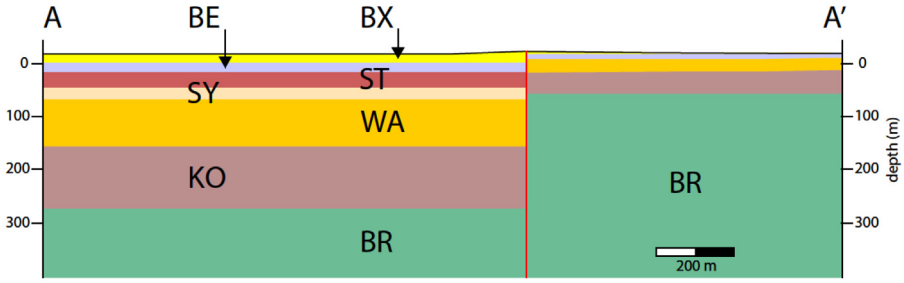


**Fig. 3.** Schematic geological cross-section showing the fault offset in Miocene (BR), Pliocene (KO) and Quaternary (WA, SY, ST, BE, BX) deposits. BE is Beegden Formation, BX is Boxtel Formation. Vertical axis in m below the Dutch ordnance datum, NAP. The cross-section is obtained from the national 3D subsurface model DGM v2.2.

discontinuous and stepped. The terrain steps can be obscured by man-induced leveling that occurred over the last centuries, but also by natural features such as wind-blown landforms (Van Balen et al., 2005). The position of faults can also be inferred from steps in the phreatic groundwater level. This has been attributed to fault sealing due to clay smearing, sand grain re-orientation and iron-oxide precipitation (Bense et al., 2003).

The selected trench location was across a terrain step (identified using a high resolution LiDAR DEM, www.ahn.nl), a change in stratigraphy, and a groundwater level step (~2 m height change) inferred from a handcoring transect. Because their locations did not coincide, it was decided to open a trench covering the scarp as well as the groundwater level step and the change in stratigraphy. In the trench it was found that the scarp is aeolian, formed by drift-sand deposition. The trench had a length of 52 m and was positioned in asymmetric layout perpendicular across the fault. The trench extended 40 m into the foot wall and 12 m into the hanging wall.

The DGM v2.2 subsurface model (www.dinoloket.nl) shows that, at the trench site, the top of the Miocene sequence (top of the Breda Formation) is offset by 220 m and the top of the Middle Pleistocene Meuse deposits (Beegden Formation) by about 24 m (Fig. 3). However, the latter maybe has to be revised based on the results presented in this paper. The DGM model is based on regional good and high quality borehole data. An artefact of this 3D model is that faults are depicted as vertical.

During the first phase of digging, the trench was excavated to the depth of the natural groundwater level (Fig. 4), which varies between 2.8 and 1.6 m depth below the undulating surface on the foot wall, and 3.7 m on the hanging wall. During the second phase, continuous pumping allowed for deepening the foot wall part of the trench by another ~2 m. During both phases the positions of marker beds were labelled and measured with dGPS. Lacquer peel profiles were made after studying the trench stratigraphy, sedimentology and structures.

### 3.2. OSL dating

Eleven samples (Bak 1–9, Bax 1–2) for optically stimulated luminescence (OSL) dating were taken at the site, to determine the time of deposition and burial of sediments. Samples were obtained by hammering opaque PVC tubes horizontally into the exposure; sample locations are indicated in Figs. 2 and 5, S1.

Under safelight conditions of the laboratory of the Netherlands Centre for Luminescence dating (located at Wageningen University & Research), sample tubes were opened. Light-exposed material from the outer ends of the tubes was prepared for dose rate estimation (ionizing radiation received by the sample per year, in Gy/ka), while material from the inner part of the tube has remained shielded from light, and is suitable for luminescence analysis to determine palaeodoses (amount of ionizing radiation received by the mineral grains since burial, in Gy). The depositional age was obtained by dividing palaeodose by dose rate for each of the samples (see e.g. Rhodes, 2011, for more information on luminescence dating). Eight samples were dated using the OSL signal of sand-sized quartz grains, while for three other samples the deposits were too old for quartz OSL dating, and luminescence signals of sand-sized feldspar grains were used.

#### 3.2.1. Dose rate

Activity concentrations of $^{40}$K and several nuclides from the Uranium and Thorium decay chains were measured using a high-resolution gamma ray spectrometer. Results were combined with information on burial history, water and organic content history, and the grain size fraction used for luminescence measurements to calculate the effective dose rate. For the feldspar extracts, an additional contribution from internal potassium and rubidium is included (see Kars et al., 2012, for details).

For calculating the cosmic dose rate we assumed immediate burial of the samples to the present depth below the surface for all samples apart from Bak1, -2 and -3, which are from older deposits that were gradually buried over time. In order to calculate water attenuation of dose rate, the minimum water content was measured on the samples as received in the laboratory. However, the samples were obtained in a drained trench. Therefore, a higher water content was assumed based on porosity estimates and the position of the phreatic groundwater level before the trench was opened, see Table 1. A peaty top soil at the footwall suggests that Holocene water levels were even higher than in the most recent decades. Attenuation of dose rate due to organic material was also taken into account, although organic contents were low (<0.5% by weight) for all samples but sample Bak4 (1.5% by weight). There were no signs of disequilibrium in the Uranium decay chain.

Several samples were taken close to stratigraphic boundaries, and especially the lower loamy unit differed considerably in radionuclide activity concentration compared to the sandier deposits. As the gamma dose rate experienced by samples comes from a sphere of up to 30 cm around the sample position, a detailed analysis was made to take into account contributions of adjacent layers (following Aitken, 1985; Wallinga and Bos, 2010). This resulted in a minor adjustment (up to 6%) of the dose rate estimate for samples taken nearby stratigraphic boundaries.

Resulting dose rate values range from 0.70 to 1.78 Gy/ka (see Table 1). Dose rates on most samples are relatively low, but in line with earlier estimates on similar deposits from this area (see e.g. Schokker et al., 2005).

#### 3.2.2. Palaeodose

Quartz is normally the mineral of choice in optical dating as its

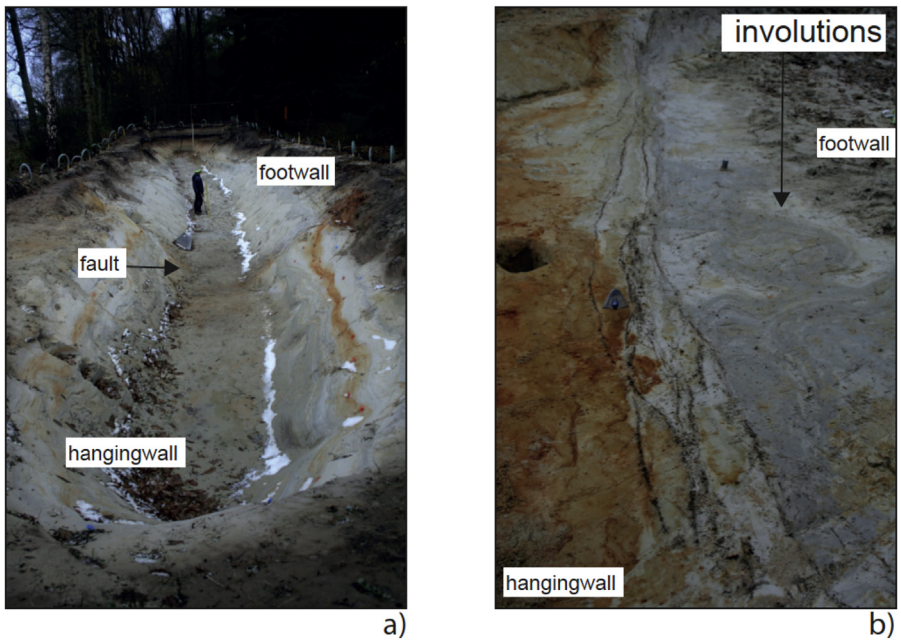


**Fig. 4.** a) Overview photo of the trench. The view is to the north, towards the footwall. The total length of the trench is about 50 m. The iron-oxide precipitation is located on the hanging wall. b) Photo of the trench floor at the fault location after completion of the first excavation stage. Footwall is on the right. The cryoturbations on the footwall side are sharply cut by the fault branches. The number of fault branches is decreasing in the viewing direction (northwest). The trowel indicates the scale.

**Table 1**
OSL results.

| NCL code | Sample | X | Y | Depth (m) | Water content (% weight) | Paleodose (Gy) | Dose rate (Gy/ka) | Age (ka) | Comments[a] | Unit |
|---|---|---|---|---|---|---|---|---|---|---|
| 24 | Bak6 | 180068 | 391015 | 0.95 | 6 ± 1.2 | 11.4 ± 40.4 | 0.85 ± 0.6 | 13.4 ± 0.6 | CAM(OD 15%) | D |
| 23 | Bak5 | 180068 | 391015 | 1.23 | 20 ± 4 | 10.1 ± 0.4 | 0.63 ± 0.02 | 16.0 ± 0.8 | CAM (OD 17%) | B |
| 22 | Bak4 | 180068 | 391015 | 1.58 | 30 ± 6 | 25.6 ± 1 | 1.73 ± 0.08 | 14.8 ± 0.9 | CAM (OD 20%) | B |
| 21 | Bak3 | 180068 | 391015 | 1.88 | 20 ± 4 | 449 ± 28 | 1.57 ± 0.1 | 286 ± 25 | FS pIRIR290 no fading correction | A |
| 20 | Bak2 | 180068 | 391015 | 2.78 | 20 ± 4 | 399 ± 28 | 1.44 ± 0.1 | 277 ± 27 | FS pIRIR290 no fading correction | A |
| 19 | Bak1 | 180068 | 391015 | 2.78 | 20 ± 4 | 377 ± 23 | 1.44 ± 0.1 | 262 ± 24 | FS pIRIR290 no fading correction | A |
| 25 | Bak7 | 180059 | 390980 | 1.01 | 4 ± 0.8 | 9.8 ± 0.4 | 0.85 ± 0.03 | 11.6 ± 0.6 | CAM (OD 15%) | D |
| 26 | Bak8 | 180059 | 390980 | 1.39 | 30 ± 6 | 13.4 ± 0.6 | 0.83 ± 0.03 | 16.1 ± 1.0 | CAM (OD 19%) | D |
| 27 | Bak9 | 180059 | 390980 | 1.86 | 30 ± 6 | 15.0 ± 0.8 | 0.98 ± 0.04 | 15.3 ± 1.0 | CAM excl. 1 outlier (OD 20%) | B |
| 29 | Bax2 | 180065 | 390988 | 1.50 | 20 ± 4 | 12.0 ± 0.5 | 0.94 ± 0.03 | 12.7 ± 0.7 | CAM (OD 15%) | C |
| 28 | Bax1 | 180065 | 390988 | 1.90 | 20 ± 4 | 13.3 ± 0.5 | 0.92 ± 0.03 | 14.3 ± 0.8 | CAM excl. 1 outlier (OD 18%) | C |

[a] CAM means Central Age Model (Galbraith et al., 1999) is used to obtain the palaeodose from the single aliquot equivalent dose distribution; the OD denotes the overdispersion in this distribution (e.g. scatter that is not explained by measurement uncertainties). X and Y are coordinates system in the Dutch National Grid (RD).

OSL signal is most rapidly reset and the signal is stable over geological time (Wintle, 2008). However, disadvantage of using the quartz OSL signal, is that it saturates at relatively low doses and hence can only be applied to relatively young deposits (~last 100 ka). Samples obtained from the Beegden Formation are expected to be older; for these samples the recently developed pIRIR dating of feldspars is used (Thiel et al., 2011). This method largely overcomes age-underestimation problems associated with anomalous fading of feldspars (e.g. Wallinga et al., 2007), and has been shown to provide accurate ages for deposits up to ~450 ka (Kars et al., 2012; Buylaert et al., 2012).

Samples were sieved to obtain the grain size fraction of 212–250 μm, and treated with HCl and $H_2O_2$ to remove carbonates and organic material. For samples Bak1, -2, and -3 the obtained fraction was then density separated at $\rho = 2.58$ kg/dm$^3$ to separate potassium-rich feldspar (light fraction) from other minerals. Quartz extracts were obtained by treating the sieved and chemically cleaned sample with 40% HF, which serves to dissolve other minerals and etch the quartz grains. This fraction was rinsed with HCl.

The Single Aliquot Regenerative (SAR) dose procedure was used for palaeodose estimation in both quartz (Murray and Wintle, 2003) and feldspar (Wallinga et al., 2000; Thiel et al., 2011). All luminescence measurements are performed on a Risø TL/OSL reader (type DA20).

For the measurements on quartz extracts, the most light-sensitive OSL signal of quartz grains is selected using the 'Early Background' approach (Cunningham and Wallinga, 2010). A pre-heat of 260 °C and a cut heat of 220 °C were selected based on the preformed pre-heat plateau dose recovery. Dose response curves obtained by fitting an exponential plus linear fit through regenerative dose OSL responses showed relatively rapid saturation, with an average $D_0$ value of 41 ± 7 Gy. An excellent dose recovery ratio of 1.023 ± 0.008 (n = 48) provides confidence in the adopted procedure. All palaeodose estimates of quartz OSL dated samples are smaller than the $2 \times D_0$ criterion (Wintle and Murray, 2006), indicating that the samples are suitable for reliable quartz OSL dating. To obtain a good estimate of the burial dose, measurements are repeated on at least 20 aliquots per sample. Each of these aliquots consists of a sample disc containing about 15–60 grains (2-mm or 1-mm diameter sample). Equivalent doses measured on the single aliquots showed scatter as expected for well-bleached deposits, with overdispersion values between 15 and 20%. For samples Bak9

and Bax1, a single outlier was excluded to avoid bias in results. Using the Central Age Model (CAM; Galbraith et al., 1999) the palaeodose is obtained from the single-aliquot equivalent dose distribution.

The feldspar pIRIR SAR protocol involves a 60s preheat to 320 °C for both the regenerative and test doses. First IR stimulation was at 50 °C for 100s, while the second stimulation (the pIRIR signal used for dating) was at 290 °C for 100s. At the end of each SAR cycle, the signal was reset by an additional 40s IR bleach at 330 °C. This protocol was also tested using a dose-recovery test. After subtraction of doses remaining after 48 h bleaching in a SOL2 solar simulator, a dose recovery ratio of 1.09 ± 0.05 is obtained. Although less good than for quartz, such dose recovery is still regarded acceptable (Yi et al., 2016).

To obtain an accurate fit of the data, the pIRIR dose response curves were fitted with a general order single-saturating exponential function (Guralnik et al., 2015). Given the time-consuming nature of the measurements, a limited number of twelve aliquots were measured per sample. Results were accepted if recycling was within 10% and recuperation was below 10%. All single aliquot dose response curves for each of the samples were cast on a standardised growth curve obeying General Order Kinetics (Guralnik et al., 2015), and simultaneously fitted to obtain un-weighted mean and standard error of the trap filling (in each sample), to be further converted to age assuming a residual dose (at burial) of 30 ± 15 Gy, commonly used for high-temperature post IR-IRSL protocols (e.g. Joordens et al., 2014). Within the luminescence community there is a debate whether pIRIR290 signals should be corrected for fading (see e.g. Kars et al., 2012). Here no fading correction was applied; this implies that the true burial ages for samples Bak1, -2, -3 may be slightly larger than those presented here.

### 3.3. Radiocarbon dating

Samples for $^{14}C$ dating (Fig. 5: C1-2) were wet sieved over a 200 μm mesh in the laboratory. Subsequently, botanical macrofossils (*Carex* seeds,1 sample) and bulk plant remains (1 sample) were extracted from the remaining sample material by use of a binocular microscope. The macro remains were (AMS) radiocarbon dated and calibrated at the Beta Analytic laboratory (Miami, Florida) using the Intcal13 curve (Reimer et al., 2013).

## 4. Results

### 4.1. Local stratigraphy and chronology

The sedimentary sequence which was exposed in the trench can be grouped into four units (Fig. 5). The boundaries between these units are defined by lithological changes and the occurrence of two marker horizons: a gravel bed and a paleosol. At and near the surface the stratigraphic succession has been disturbed by digging (mainly footwall), levelling (hanging wall) and by a man made structure consisting of an earthen wall bordered by two ditches (a "landweer" or "landwehr"; defense construction; dating probably from the 14th century).

#### 4.1.1. Unit A

Unit A is the lowest of the four units and consists of a heavily deformed mixture of whitish coarse sand beds with isolated gravel pockets, gravel strings (thin gravel beds) and grayish loam layers (Fig. 5). The gravels consist of milky quartz, flints, sandstones and quartzites. A continuous gravel layer with clasts up to 10 cm in size is present at, and sometimes close to, the top of the unit. Next to the fault, part of the deformed loam layers have dark brown to purple black colors. SEM and TXRF analyses showed the presence of relatively large amounts of carbon (J. Griffioen, pers. comm., 2015). OSL dating of unit A shows age ranges of 286 ± 25 to 262 ± 24 ka (Table 1).

Based on the gravel composition and lithology, we interpret unit A as Meuse deposits of the Beegden Formation. The loam layers with relatively large amounts of carbon may represent the remains of paleosols. The gravel string near the top of the unit is likely a gravel lag reflecting an erosional unconformity. The interpretation and OSL-determined age are in agreement with the local geology (Schokker et al., 2007). Given its age and the erosional unconformity, unit A must have experienced periglacial conditions multiple times, and the intense deformations can therefore be attributed to cryoturbation processes. However, some of the deformations are very large and vertically straight, and could, therefore, represent earthquake related fluidization features.

#### 4.1.2. Unit B

This unit consists of alternating layers of gray sandy loam and yellowish fine sand. The base of the unit is formed by an abrupt transition to the gravelly sands of unit A. The thickness of unit B varies between ~0.4 and 1 m, being thickest on the hanging wall. The loamy sediments have an average median grain size of about 70 μm, the fine-sandy deposits have a grain size of about 165 μm. In Fig. 5 we have discriminated a lower loamy sub-unit and a sandy upper sub-unit. The loamy sub-unit is more sandy in the central part of the trench section, where also the number of intercalated sand layers within the sub-unit is larger. Locally, the basal, loamy part of the sub-unit contains humic intervals (Fig. 5). On the foot wall, the sandy sub-unit contains 0.33 m high fore-sets, prograding towards the fault. The unit is heavily deformed, most intense towards the base, mainly in the form of meter-scale involutions (Figs. 4b and 5). Brittle deformation of the unit can be seen along the fault structure. On the hanging wall the sediments are also deformed by small scale flame structures (Fig. 6b).

Two radiocarbon datings were performed on the same humic interval (Fig. 5: C1-2). The sample on bulk plant remains resulted in a calibrated age of 14535–14090 cal yr BP (95.4% probability; conv. age 12320 ± 30 BP; sample number Beta-517496). The sample on *Carex* seeds resulted in an age of 14276–13991 cal yr BP (95.4% probability; conv. age 12230 ± 40 yr BP; sample number Beta-512656).

OSL dating results for the basal sub-unit range from 15.3 ± 1.0 ka to 14.8 ± 0.9 ka (samples Bak9 and 4). The OSL result for the upper sub-unit is 16.0 ± 0.8 (sample Bak5), whereas an OSL date of 16.1 ± 1.0 was obtained just above its upper boundary, close to the contact with unit C (sample Bak8). Clearly, the OSL age constraints for the upper sub-unit are slightly too old. This might be an effect of changing water saturation conditions. The involutions are syn-depositional, and contain the humic intervals in their cores. They are interpreted as cryoturbations. The fore-sets in the sandy-subunit on the foot wall indicate a shallow lake environment with a small delta. Combined, the grain size of the sediments, the sedimentary facies, the periglacial deformations and presence of *Carex* seeds indicate that the most likely paleo-environment of unit B is aeolian deposition in thaw lake(s) developing on a degrading permafrost. Based on the lithology, the age, the cryoturbations and the interpretation of the overlying unit C (see below), we propose that unit B can be correlated to the Lower Loamy Bed, which is of Bølling age (~14.7–14.0 ka; Vandenberghe et al., 2013).

#### 4.1.3. Unit C

The sequence of unit C consists of fine and coarse gravelly sands, intercalated with thin gravelbeds. The average gravel size is a few mm's, the maximum size is about 1 cm. On the hanging wall the unit is wedge-shaped, having a thickness of ~1 m at the fault

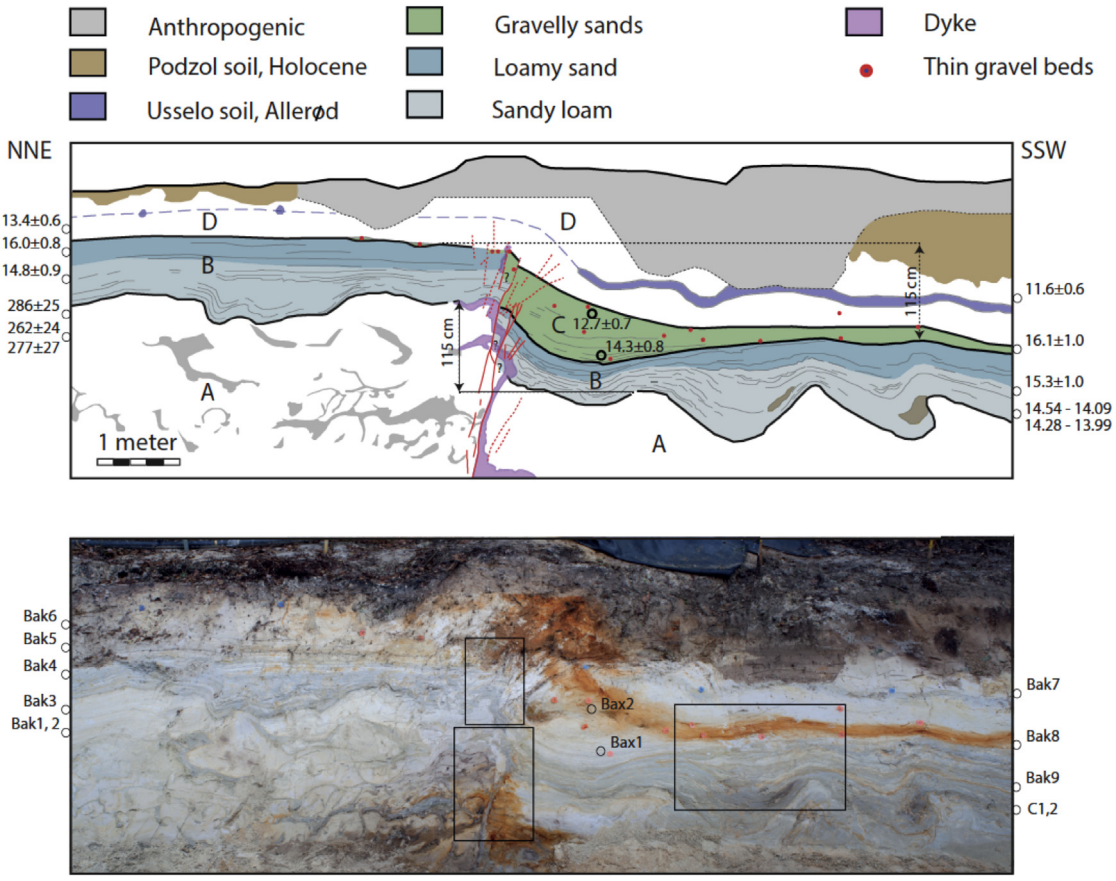


**Fig. 5.** Photo composite (below) and interpretation (top) of the eastern trench wall with OSL dating results in ka and $^{14}C$ in calibrated ka BP. Red lines indicate faults (continuous lines) and cracks (dashed lines). The pink colour represents a large clastic dyke along the fault planes. The other colors represent stratigraphic units. Red dots symbolize thin gravel layers (gravel strings). Two OSL samples were taken in the imaged part of the trench (Bax1, Bax2). Results of nine additional OSL samples located in other parts of the trench (Fig. 2f, Supplementary Fig. 1) could be extrapolated to this part based on the stratigraphic positions and markers. The rectangles in the centre represent the positions of the two lacquer peel profiles (Supplementary Fig. 2), the rectangle on the right shows the location of Fig. 6a. . (For interpretation of the references to color in this figure legend, the reader is referred to the Web version of this article.)

contact and tapering to a thickness of a gravel string away from it (Fig. 5). The wedge on the hanging wall is composed of multiple depositional sequences separated by erosional unconformities. On the footwall the unit has a thickness of one gravel string.

The results from $^{14}C$ dating in the underlying unit indicate an age for this unit which is younger then Bølling (~14.7–14.0 ka). The OSL derived age for the base of unit C is 16.1 ± 1.0 (Bak8), which is slightly too old (see above). Ages of the two OSL samples in unit C are 12.7 ± 0.7 ka (Bax2) and 14.3 ± 0.8 Ka (Bax1).

The grain size, gravel content, bedding and unconformities point to deposition by shallow waterflow in a colluvial wedge. The unit's faulted base and wedge-shape geometry on the hanging wall indicates syn-tectonic sedimentation. We tentatively propose that deposition has taken place during the Older Dryas (~14.0–13.9 ka), which is characterized by a relative open landscape with sparse vegetation, leading to renewed aeolian deflation and deposition (Hoek and Bohncke, 2002). The thin gravel bed can be interpreted as a deflation lag, comparable to the Beuningen Gravel Bed. However, its age is younger than the age of the Beuningen Gravel Bed according to Vandenberghe et al. (2013), since it overlies unit B of Bølling age.

### 4.1.4. Unit D

The sediments of unit D consist of horizontally bedded, well-sorted sand with a median grain-size of approximately 175 μm. On the hanging wall a ~15 cm thick, gray, sandy loam (median grain size about 65 μm) with charcoal particles occurs in this unit (Fig. 5). On the footwall a very discontinuous bleached level with a mottled appearance is present. The bleaching locally extends to more than one meter deep, probably following the paths of decayed roots. The Holocene soil in the top of the unit has been heavily disturbed by digging. At the northern part of the foot wall, the soil has a peaty appearance indicating wet conditions with a high groundwater level. At the hanging wall, in terrain with lower groundwater levels, the Holocene soil typically is a well-defined podzol.

OSL ages obtained for unit D are 13.4 ± 0.6 ka (sample Bak6, below the gray loam) and 11.6 ± 0.6 (sample Bak7, above the gray loam).

We interpret the sediments of Unit D to correspond to the dry aeolian sand sheet deposits of the Younger Coversands I and II (Kasse et al., 2007; 'Facies A' by Schokker and Koster, 2004). The overall characteristics and age of the gray sandy loam show strong similarities to the Usselo soil, which has developed during the Allerød and early Younger Dryas. The bleached and mottled discontinuous level on the foot wall may represent remnants of a soil of the same age, but formed in different wetness conditions compared to the hanging wall. The Usselo soil separates the Younger Coversands I and II in unit D.

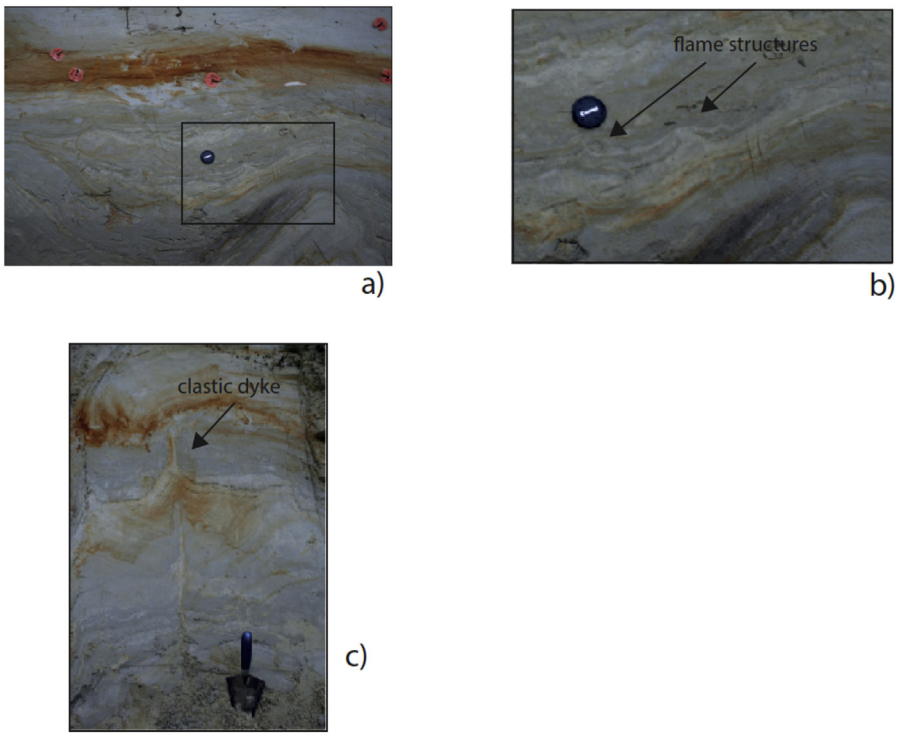


**Fig. 6.** a,b) flame structures in unit B on the hanging wall. The location is depicted in Fig. 5 c) dyke injecting through loamy parts of unit B and truncated by unit C. The sediment covering the top of this dyke has been dated by OSL (sample Bak8).

### 4.2. Structural observations

#### 4.2.1. Tectonic features in the fault zone

In the trench, a ~1 m wide fault zone was exposed, consisting of major and minor faults with displacement, and deformation bands (Fossen et al., 2007; Brandes and Tanner, 2012) without (significant) displacement (Figs. 5 and 7). No other faults were found in the trench, which extended 40 m in to the foot wall and 12 m into the hanging wall (Figs. 2 and 4). On the eastern wall of the trench the fault zone is near-vertical and splays upwards (Fig. 7). Here the lowest exposed part consists of one major fault and sub-parallel secondary faults. The orientations in the middle part of the major fault are (dip direction/dip angle) 230/90, 225/85, 050/85; in the basal part they are 220/70, 230/85 and 050/70. On the western side of the trench the fault zone has a 60° dip (fault plane orientation in the basal part is 240/60), and consists of two major, parallel fault planes. At the trench floor a smooth, gradual transition from the near vertical and splaying to the straight and 60° sloping character was visible in planform (Fig. 4b).

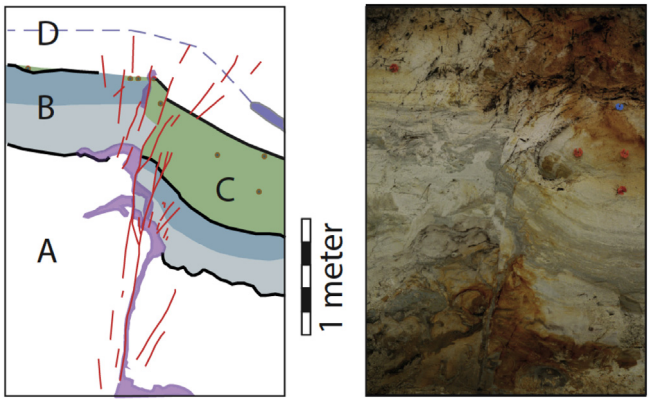


**Fig. 7.** Photo (right) and interpretation (left) of the fault zone. The faults (straight red lines) are steep and splay upwards. A clastic dyke (purple) intruded upwards along the faults. The top of the dyke could not be determined. (For interpretation of the references to color in this figure legend, the reader is referred to the Web version of this article.)

The main and secondary faults cut straight through the loam layers of unit A, without indications for smearing or dragging (Figs. 5 and 7). Both the top and the base of unit B are displaced along the fault zone by about 1.15 m (Figs. 5 and 7). Cryoturbation structures in unit B are abruptly cut off by the faults, also without dragging or smearing. This was visible in profile as well as in planform on the trench floor after the first excavation stage (Fig. 4b). In addition, no evidence for lateral displacements could be found in the faulted cryoturbations on the trench floor. On the hanging wall unit C has a wedge shape, indicating it was deposited against a fault scarp. On lacquer peel profiles (supplementary Fig. 2) gravels of unit C were traced in the fault zone, indicating a small displacement of the top of unit C of maximum 0.2 m. Based on the geometry of unit C (Figs. 5 and 7), the displacement could be a bit less, around 0.1 m. The Usselo soil in unit D could not be traced in the fault zone due to overprinting by gleyic phenomena (oxidation; see Figs. 5 and 7). However, the characteristics of the soil on the hanging wall differ from those of the foot wall. On the hanging wall, it is a ~15 cm thick, gray sandy loam, whereas on the footwall it is a very discontinuous bleached, mottled level. This confirms that the fault scarp relief existed during the period of soil formation. However, it was not possible to determine if the soil experienced faulting.

#### 4.2.2. Flame structures

Upward-directed intraformational, cm-scale fold structures occur within the deposits of unit B. They are mainly situated on the south flanks of the involutions located directly next to the fault

zone (Fig. 6a and b). They have a flat base and fade out in upward direction (cf Vanneste et al., 1999). Their intraformational position indicates that they postdate the deposition of unit B. In paleoseismological studies such flame structures are attributed to (pore) water escape induced by seismic shaking (Vanneste et al., 1999). However, the periglacial conditions during and after the deposition of unit B implies that they could also be the relicts of ice lenses (Vandenberghe, 2006).

#### 4.2.3. Clastic dykes

A large dyke is situated in the fault zone (see Figs. 5 and 7). The material of this dyke consists of loamy fine sand. On lacquer peel profiles the dyke shows faint flow lineations, indicative of upward injection of sediment, aligned parallel to the dyke orientation (Supplement Fig. 2). The base of the dyke is below the trench floor (Fig. 7). The dyke is aligned subparallel to the main fault through unit A, but higher upwards the pathway of the dyke becomes irregular. It more or less follows the faults of the fault zone, but switches between fault branches, and also intrudes laterally in to the host sediment. The exposure in the trench and the detailed lacquer peel profiles both showed that the dyke is non-faulted. Small secondary thrust faults in the surrounding sediments originate from the dyke, and can be linked to the intrusion process. On the upper lacquer peel profile (Supplement Fig. 2a and b), the upper part of the dyke can be traced along a fault separating unit C (hanging wall) from unit B (foot wall), in to deposits overlying the gravel strings of unit C, i.e. the base of unit D. Due to subrecent anthropogenic disturbance of the topsoil it was not possible to determine if the upper part of the dyke cuts through the Usselo soil. Lacquer peel profiles of the faults on the western trench wall show that dyke injections are here also present along the faults and cracks, but much thinner (cm's, mm's). On the trench floor the dyke was parallel to the fault zone (Fig. 4b).

Two small clastic dykes were present within unit B: one in the foot wall, and one in the hanging wall (Fig. 6c). The dyke on the foot wall is 0.4 m high; its loamy source layer is characterized by flame structures. The dyke on the hanging wall is 0.6 m high. Both dykes have a maximum width of 2 cm and have near vertical orientations (strike orientation on the foot wall N320-140E, N060-240E on the hanging wall). Both dykes are truncated by a gravel string of unit C, which provides a minimum age for the dykes. OSL sample Bak8 ($16.1 \pm 1.0$ ka) was taken directly above the dyke in the hanging wall (Supplement Fig. 1e). In addition, the dyke on the foot wall is clearly overprinted by biogenic mottling, the result of dung beetle burrowing in the Usselo soil.

## 5. Discussion

### 5.1. Timing of faulting events

The cryoturbations in unit B developed syn-sedimentary. They show limited asymmetry in cross-section (Fig. 5). In addition, planform sections exposed at the trench floor show semi-circular- to oval-shaped geometries (Fig. 4b). Thus, they were formed in the absence of a significant slope, which implies that there was no fault scarp present during deposition of unit B. Additionally, the sedimentary environment interpreted for unit B (shallow lakes/ponds) implies a negligible surface slope, and thus a levelled surface without a fault scarp. Both the top and the base of unit B are displaced along the fault zone by about 1.15 m (Figs. 5 and 7). This confirms that all the observed fault offset of unit B post-dates its deposition. However, the basinward (from footwall to hanging wall) thickening of unit B does imply a slight syn-sedimentary tilting. In contrast, the thickness variation in unit C shows that this unit was deposited on a faulted relief; the thickest part is interpreted as a colluvial wedge deposited in front of a fault scarp. The base of unit C is displaced 1.15 m; the top of the unit shows limited offset (0.2–0.1 m). Thus, the main displacement (0.95–1.05 m) has taken place just before deposition of unit C.

### 5.2. Clastic dykes

In general, clastic dykes are created by injection of a fluid with sufficient pressure to allow for fracture creation in and dilation of overburden, and for flow of a sand-fluid mixture. The exerted pressure must have been larger than the hydrostatic pressure, and the resulting flow needs to be fast enough to create drag forces larger than the effective weight of the entrained grains (Lowe, 1975; Obermeier, 1996). Earthquakes can create this required overpressure by shear stresses causing compaction due to rearrangement of sand grains, in an attempt to gain a more dense packing (Obermeier, 1996). The threshold values of magnitudes and intensities of earthquakes for fluidization is 4.2 (Ms), respectively 5.5 (MCS), for epicentral distances of <10 km (Galli, 2000; Cox et al., 2007). One large and two small clastic dykes were present in the trench. The two small dykes within unit B are overlain by a gravel string of unit C, and thus predate formation of unit D. They may have been coeval with the 0.95–1.05 m faulting event. For the largest dyke the position of the top could not be determined; the highest traceable position is just above the gravel strings of unit C on the upper lacquer peel profile (Supplement Fig. 2a and b). This dyke is not faulted, although it is situated in the core of the fault zone. Most likely the large dyke is related to the second event and was formed during or immediately following the offset of 0.2–0.1 m.

### 5.3. Creep versus surface rupture

Fault displacements observed in trenches or inferred from morphology can be caused by sudden seismogenic rupture or by more progressive failures related to fault creep (e.g. Ahorner, 1962, 1975; McCalpin, 1996; Houtgast et al., 2003, 2005; Van Vliet Lanoë et al., 2004; Burbank and Anderson, 2011). For the fault displacements in the RVRS both models have been advocated in various studies. The lack of historic surface ruptures, combined with the fact that present-day vertical motions (inferred from geodetic measurements) occur without accompanying earthquakes, suggest that the fault creep model applies to a number of studied faults in the RVRS (Ahorner, 1962, 1975; Houtgast et al., 2003, 2005; Demoulin, 2006). However, Camelbeeck et al. (2007) and Grützner et al. (2016) argue that the lack of historic surface ruptures can also be explained by a low re-occurrence interval, and insufficient magnitudes and large focal depths of the historic earthquakes, in combination with the relatively short period of historic observations. Furthermore, the observed present-day geodetic motions around faults can also be induced by differential man-induced groundwater level changes (Vanneste and Verbeeck, 2001; Camelbeeck et al., 2007; Caro Cuenca, 2012), and thus unrelated to active creeping fault displacement. On the other hand, there is evidence for seismogenic surface rupturing in trench studies in the RVRS, in the form of colluvial wedges, liquefactions, linear extensional fissures and mass wasting. In addition, absence of evidence for syn-sedimentary (growth-) faulting (in trenches) shows that the faults do not displace slowly, by creep (Camelbeeck et al., 2007). Houtgast et al. (2003, 2005) found fluidizations, mass wasting (solifluction lobes), and episodic fast fault displacements rates. Based on this, they concluded that evidence for a paleo-earthquake was present in the trenches they studied. However, they also concluded that there was no firm evidence for paleo-surface rupture(s), for the following reasons: 1) As shown by the 1992

Roermond earthquake, fluidizations can be caused by non-surface rupturing earthquakes. 2) Earthquake-induced fluidizations encountered in a trench are not necessarily related to the trenched fault; the causative fault can, in theory, be at some distance. 3) In the study area, mass wasting does not provide conclusive evidence for an earthquake because it is also a common feature in periglacial environments (solifluction) during which the trenched sedimentary sequences were formed. They only require a small slope and a frozen subsurface to occur. In addition, Demoulin (2006) found evidence for slow movements along the FFZ (trenched by Houtgast et al., 2003, 2005) by analyzing geodetic data. However, these displacements can also be explained as vertical movements caused by mining-induced subsidence (Caro Cuenca, 2012).

In the Bakel trench presented in this paper we found several convincing indications for seismogenic surface rupturing. First, the fault cuts sharply through the involutions of unit B, and the loam layers of units A and B. This indicates a sudden, rapid displacement (i.e. a high strain rate; c.s.. Verbeeck et al., 2017). The wedge-shape of unit C has no evidence for significant growth faulting, which indicates a 0.95–1.05 m high fault scarp was formed in a very short period of time. A displacement of ~1 m corresponds to an earthquake magnitude $6.8 \pm 0.3$ (Wells and Coppersmith, 1994; Camelbeeck et al., 2007). A second rupture event is evidenced by the 0.2–0.1 m displaced top of unit C. The three clastic dykes are also evidence for paleo-earthquake(s). Although the dykes do not proof that earthquakes took place along the specific fault zone exposed in the trench, the fact that a major dyke even intruded along the fault planes provides circumstantial evidence. Finally, the splaying of the fault zone towards the top, a common observation in many trenches in the RVRS (Houtgast et al., 2003; Camelbeeck et al., 2007; Grützner et al., 2016; Verbeeck et al., 2017), can be explained by a decrease of confining pressure towards the surface during a rupturing event in unconsolidated sediments (McCalpin, 1996; Verbeeck et al., 2017).

### 5.4. Relation of the fault to the local topography

A scarp is present at the trench site, but this elevation change does not coincide with the location of the fault. Examination of the upper parts of the exposed sequence in the trench shows that below the scarp aeolian deposits occur above a well-defined Holocene podzol soil. Although these deposits are not OSL dated, they are very likely Medieval in age due to the preserved traces of peat digging in the Holocene peaty soil below the wind-blown sands. This is reinforced by historic descriptions of large-scale drift-sand activity around (and even in) the town of Bakel. In conclusion the current terrain step north of the fault is not tectonic by nature but the result of aeolian, drift-sand deposition.

### 5.5. Sequence of events

The reconstructed sequence of events is depicted in Fig. 8. The evolution of the sequence exposed in the trench starts with the sedimentation of Meuse (fluvial) deposits around ~260 ka of unit A. Following a long time of soil formation, erosion and/or non-deposition (only the gravel lag is preserved), unit A is buried by the reworked aeolian and lacustrine deposits of unit B (Fig. 8b). This unit was deformed by cryogenic processes during final permafrost degradation in the Bølling period. During its deposition no fault scarp and no significant surface slope was present in the landscape. The main seismic event, with 0.95–1.05 m displacement, took place before unit C was deposited (Fig. 8c). This unit reflects sedimentation against the scarp, in a colluvial wedge formed by fluvio-aeolian sedimentation and deflation processes shortly after the Bølling period. The configuration of the unit against the scarp does not show evidence for scarp erosion, which might be explained by frozen conditions (permanent or seasonal) during the Older Dryas, when unit C was likely deposited. Such periglacial conditions are also required for surface wash to occur on these sandy deposits. A second, smaller seismic event, leading to an additional 0.2–0.1 m displacement, occurred after deposition of unit C (Fig. 8d). During this event the main clastic dyke intruded along fault branches in the fault zone (Fig. 8e). Finally, the faulted topography is buried by aeolian unit D with the intercalated Usselo soil of Allerød age (Fig. 8f). During construction of the landwehr on top of the fault zone in Late Medieval times, the fault relief has been destroyed. The present-day landscape shows a terrain step 25 m away from the fault, on the foot wall, caused by drift sand deposition.

### 5.6. Comparison to other trenching results along the PBFZ

Van den Berg et al. (2002) studied a trench across the Peel Boundary fault zone, near the town Neer, located 32 km to the southeast of Bakel (Fig. 2a). Three faults were exposed in their trench, showing a total displacement of 0.9 m. As argued below, the two events they found likely have similar ages as the two events in our trench. The observed stratigraphy in the Neer trench is similar (M. Van den Berg, pers. comm., 2014, 2018). For their hanging wall, Van den Berg et al. (2002) describe and draw a colluvial unit consisting of cross-bedded, coarse-grained shallow fluvial sands overlying a gravel string (Fig. 9). On the foot wall and close to the fault, the correlatable gravel string incises 0.5 m into underlying deposits, indicating that a scarp existed during the final stage of the formation of the desert pavement gravel string. The TL and IRSL ages provided in Frechen and Van den Berg (2002) indicate that the gravel string at the base of the colluvial wedge was deposited shortly after $13.7 \pm 1.6$ ka (TL) or $10.8 \pm 1.6$ ka (IRSL). On the footwall the gravel string has a maximum age of $11.8 \pm 2.1$ ka (TL) or $14.2 \pm 2.3$ ka (IRSL). These ages constrain the age of the first, 0.5 m displacement event in Neer. They are in agreement with our $^{14}C$ and OSL-based age estimate for the first event in Bakel, except for the IRSL result on the hanging wall. However, since IRSL results are nowadays in general considered unreliable, we think the correlation of the events is possible. The second event in the Neer trench, having 0.35 m displacement, is constrained by soil formation predating this event, and by the absence of deformation of a fluvial (Meuse) terrace of Allerød age near the trench site. Van den Berg et al. (2002), therefore, conclude that the second event took place during the Bølling interstadial. However, this is not possible according to the dating results presented by Frechen and Van den Berg (2002). In addition, the Allerød terrace near Roermond, at the other side of the Meuse river, does have a scarp at the PBFZ (Michon and Van Balen, 2005). Because the Allerød time-period has multiple terrace levels in this area (Van den Broek and Maarleveld, 1963; Woolderink et al., 2018), we propose that the second event was intra-Allerød (~13.9–12.85 ka); the oldest terrace level is faulted, the younger levels are not. The timing of this second event in Neer could correspond to the timing of our second surface rupture event, although in the Bakel trench the timing is not well-constrained (i.e. post-dating deposition of unit C).

In conclusion, the rupture events in the Bakel trench are likely similar to the two events documented in the Neer trench. The length of the surface rupture would then be at least 32 km, which is in agreement with the size of the magnitude based on the offset concluded in this paper for the Bakel trench (Wells and Coppersmith, 1994; Camelbeeck et al., 2007).

### 5.7. Relation to deglaciation

A previous synthesis of paleo-seismological fault-trenching

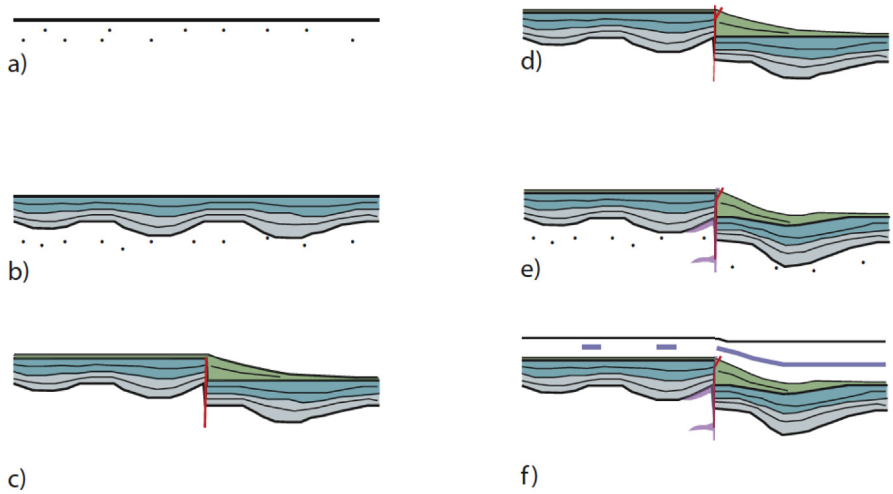


**Fig. 8.** Schematic reconstruction of events. a) Following the deposition of unit A by the Meuse river, multiple cycles of deposition, soil formation, periglacial deformation and erosion have taken place. b) Loamy and sandy sediments (unit B) were deposited and deformed by cryoturbation during the first part of the Late Glacial, in a thaw lake environment with degrading permafrost. c) A first, 0.95–1.05 m surface rupturing event took place, and gravelly coarse sands (unit C) were deposited at ~14 ka. d) The gravelly sand unit C and the base of unit D were faulted with limited offset during a second surface rupture event of at ~13 ka. e) A clastic dyke intruded along the fault structure during or immediately after the second event. f) The fault scarp was covered by aeolian deposits, including a paleosol of Allerød age (Usselo soil).

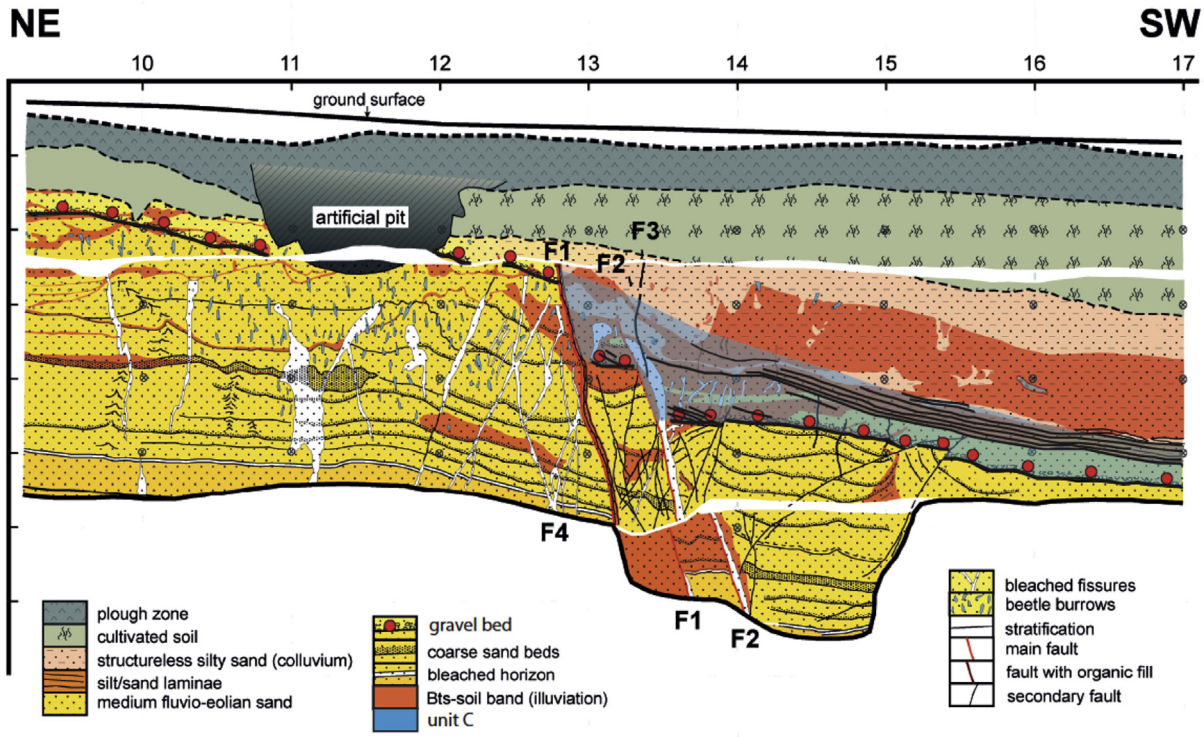


**Fig. 9.** Result of the fault trench in Neer (modified after Van den Berg et al., 2002), located 32 km to the southeast, on the Peel Boundary Fault zone (Fig. 2a). The colluvial wedge in the blue shaded part of the hanging wall is similar to our unit C. . (For interpretation of the references to color in this figure legend, the reader is referred to the Web version of this article.)

studies in the RVRS showed that most of the earthquakes occurred during the 10–15 ka time period, roughly the Weichselian Late Glacial (Houtgast et al., 2003, 2005). An exception is the Holocene surface rupturing event found in a trench across the Geleen fault, part of the Feldbiss fault zone (Vandenberghe et al., 2009; Vanneste et al., 2018). The 10–15 ka time period is in agreement with the inferred ages for the rupturing events in the trenches across the Peel Boundary fault presented and discussed in this paper. Also, fluvial deposits in the Rhine-Meuse delta, located just north of the RVRS, have been faulted during the Late Glacial (Cohen et al., 2002). The timing hints at a relation between seismicity and the Weichselian deglaciation of NW Europe. A plausible mechanism is activation of faults due to collapse of the Weichselian glacio-isostatic forebulge (Houtgast et al., 2005). Independent evidence for the existence of such a forebulge and it's collapse comes from sea-level data (Kiden et al., 2002), fluvial evolution reconstructions

(Busschers et al., 2007; Peeters et al., 2016) and glacio-isostatic modeling (e.g. Vink et al., 2007). Forebulge decay causes fiber-stresses which may stimulate the slip of faults, depending on their orientation and on the ambient plate-tectonic stress conditions (Muir-Wood, 2000; Hampel et al., 2009). This mechanism has been proposed for faults in the RVRS (Houtgast et al., 2005), and for faults closer to the former glacial margin (Mörner, 1978, 2013; Brandes et al., 2012, 2015, 2018; Jakobsson et al., 2014; Sandersen and Jørgensen, 2014; Steffen et al., 2014). For example, at a distance of 310 km south of the maximum extent of the Weichselian ice sheet, faulting and earthquakes occurred along the Osning Thrust zone (Brandes et al., 2012). The RVRS is located at a distance of 400 km to the former maximum ice-limit. If these earthquakes can indeed be attributed to a collapsing forebulge, their ages could show a decrease in the direction of ice-sheet retreat. This might indeed be the case, as the ages change from 14 ka, for the first and largest event in this trench, via 13–16 ka in NW Germany (Osning Thrust Zone; Brandes et al., 2012), to 12–14 ka in northern Denmark (Brandes et al., 2018). However, because these ages overlap, they could also be synchronous.

## 6. Conclusions

A large surface rupturing earthquake event occurred along the Peel Boundary fault zone in the southern Netherlands, around 14 ka ago. The vertical displacement of 0.95–1.05 m corresponds to an earthquake magnitude $6.8 \pm 0.3$. This was followed by a second small displacement event of 0.2–0.1 m, which, by correlation to another trench, at Neer, likely occurred around 13 ka. The second event was accompanied or followed shortly by a fluidization event, forming a clastic dyke in the fault zone. Both events can be correlated to the results of a previous trench, showing that the rupture length can have been at least 32 km, which is the along fault distance between the two trenches. These results corroborate previous results on earthquake and faulting events in the Roer Valley Rift System and Lower Rhine Embayment. The reconstructed timing of the displacement events suggests a causative link with glacio-isostatic rebound. The date of the main event fits well in a series of dates potentially showing a weak N-S trend in the age of earthquakes associated with glacio-isostatic rebound: from 14 ka, in this trench, via 13–16 ka at the Osning Thrust Zone, NW Germany, to 12–14 ka in northern Denmark. If so, this likely reflects the northward movement of the glacio-isostatic forebulge following the retreat of the Weichselian (Würmian) ice-sheet in response to climate amelioration. Our results show that fluidization can play an important role during the faulting process, whereby the fault planes themselves act as pathways for expulsion of fluidized sediment.

## Acknowledgements

Mark Kerkhoff of Waterschap Aa en Maas is thanked for his persistent efforts to get the trench permissions and logistics done. TNO colleagues are thanked for their help during the OSL sampling and the discussions in the field. Meindert van den Berg (retired), Klaus Reicherter (RWTH Aachen), Kris Vanneste and Koen Verbeeck (Observatorium Brussels) are also thanked for the discussions. We would like to thank editor O'Cofaigh and two anonymous reviewers for their positive and constructive comments.

## Appendix A. Supplementary data

Supplementary data to this article can be found online at https://doi.org/10.1016/j.quascirev.2019.06.033.

## References

Ahorner, L., 1962. Untersuchungen zur Quärteren Bruchtektonik der Niederrheinischen Bucht. Eiszeitalt. Ggw. 13, 24–105.
Ahorner, L., 1975. Present-day stress field and seismotectonic block movements along major fault zones in central Europe. Tectonophysics 29, 233–249.
Aitken, J., 1985. Thermoluminescence Dating. Academic Press, London, p. 359.
Bense, V.F., Van Balen, R.T., De Vries, J.J., 2003. The impact of faults on the hydrogeological conditions in Roer Valley Rift System: an overview. Neth. J. Geosci.-Geol. Mijnb. 82, 41–54. https://doi.org/10.1017/S0016774600022782.
Brandes, C., Tanner, D.C., 2012. Three-dimensional geometry and fabric of shear deformation-bands in unconsolidated Pleistocene sediments. Tectonophysics 518–521, 84–92.
Brandes, C., Steffen, H., Steffen, R., Wu, P., 2015. Intraplate seismicity in northern Central Europe is induced by the last glaciation. Geology 43, 611–614.
Brandes, C., Winsemann, J., Roskoch, J., Meinsen, J., Tanner, D.C., Frechen, M., Steffen, H., Wu, P., 2012. Activity of the Osning thrust in central Europe during the Lateglacial: ice-sheet and lithosphere interactions. Quat. Sci. Rev. 38, 49–62.
Brandes, C., Streffen, H., Sandersen, P.B.E., Wu, P., Winsemann, J., 2018. Glacially induced faulting along the NW segment of the Sorgenfrei-Tornquist Zone, northern Denmark: implications for neotectonics and Lateglacial fault-bound basin formation. Quat. Sci. Rev. 189, 149–168.
Burbank, D.W., Anderson, R.S., 2011. Tectonic Geomorphology, second ed. Wiley-Blackwell, p. 460.
Busschers, F.S., Kasse, C., Van Balen, R.T., Vandenberge, J., Cohen, K.M., Weerts, H.J.T., Wallinga, J., Johns, C., Clveringa, P., Bunnik, F.P.M., 2007. Late Pleistocene evolution of the Rhine-Meuse system in the southern North Sea basin: imprints of climate change, sea-level oscillations and glacio-isostasy. Quat. Sci. Rev. 26, 3216–3248.
Buylaert, J.-P., Jain, M., Murray, A.S., Thomsen, K.J., Thiel, C., Sohbati, R., 2012. A robust feldspar luminescence dating method for Middle and Late Pleistocene sediments. Boreas 41, 435–451.
Camelbeeck, T., Vanneste, K., Alexandre, P., Verbeeck, K., Petermans, T., Rosset, P., Everaerts, M., Warnant, R., Van Camp, M., 2007. Relevance of active faulting and seismicity studies to assessments of long-term earthquake activity and maximum magnitude in intraplate northwest Europe, between the Lower Rhine Embayment and the North Sea. In: Stein, S., Mazzotti, S. (Eds.), Continental Intraplate Earthquakes: Science, Hazard and Policy Issues, vol. 425. Geological Society of America Special Paper, pp. 193–224.
Caro Cuenca, M., 2012. Improving Radar Interferometry for Monitoring Fault-Related Surface Deformation. Applications for the Roer Valley Graben and Coal Mine-Induced Displacements in the Southern Netherlands, p. 142. PhD thesis TuDelft, Delft, the Netherlands.
Caro Cuenca, M., Hooper, A.J., Hansen, R.F., 2013. Surface deformation induced by water influx in the abandoned coal mines in Limburg, The Netherlands. J. Appl. Geophys. 88, 1–11.
Cohen, K.M., Stouthamer, E., Berendsen, H.J.A., 2002. Fluvial deposits as a record for Late Quaternary neotectonic activity in the Rhine-Meuse delta, The Netherlands. Neth. J. Geosci.- Geol. Mijnb. 81 (3–4), 389–405.
Cox, R.T., Hill, A.A., Larsen, D., Holzer, T., Forman, S.L., Noce, T., Gardner, C., Morat, J., 2007. Seismotectonic implications of sand blows in the southern Mississippi Embayment. Eng. Geol. 89, 278–299.
Cunningham, A.C., Wallinga, J., 2010. Selection of integration time-intervals for quartz OSL decay curves. Quatr. Geochronol. 5, 657–666.
Demoulin, A., 2006. Slip rate and mode of the Feldbiss normal fault (Roer Valley Graben) after removal of groundwater effects. Earth Planet. Sci. Lett. 245, 630–641.
Fossen, H., Schultz, R.A., Shipton, Z.K., Mair, K., 2007. Deformation bands in sandstone: a review. J. Geol. Soc. 164, 755–769.
Frechen, M., Van den Berg, M.W., 2002. The coversands and timing of late Quaternary earthquake events along the Peel Boundary fault in The Netherlands. Neth. J. Geosci.- Geol. Mijnb. 81, 61–70.
Galbraith, R.F., Roberts, R.G., Laslett, G.M., Yoshida, H., Olley, J.M., 1999. Optical dating of single and multiple grains of quartz from Jinmium Rock Shelter, northern Australia: Part I, experimental design and Statistical models. Archaeometry 41, 339–364.
Galli, P., 2000. New empirical relationships between magnitude and distance for liquefaction. Tectonophysics 324, 169–187.
Geluk, M.C., Duin, E.J., Dusar, M., Rijkers, R., Van den Berg, M.W., Van Rooijen, P., 1994. Stratigraphy and tectonics of the Roer Valley graben. Neth. J. Geosci.-Geol. Mijnb. 73, 129–141.
Grützner, C., Fischer, P., Reicherter, K., 2016. Holocene surface rupture of the Rurrand Fault, Germany- insights from paleoseismology, remote sensing and shallow geophysics. Geophys. J. Int. 204, 1662–1677.
Guralnik, B., Li, B., Jain, M., Chen, R., Paris, R.B., Murray, A., Li, S.H., Pagonis, V., Valla, P.G., Herman, F., 2015. Radiation-induced growth and isothermal decay of infrared-stimulated luminescence from feldspar. Radiat. Meas. 81, 224–231.
Hampel, A., Hetzel, R., Maniatis, G., Karow, T., 2009. Three-dimensional numerical modeling of slip rate variations on normal and thrust fault arrays during ice cap growth and melting. J. Geophys. Res.– Solid Earth 114, B08406. https://doi.org/10.1029/2008JB006113.
Hoek, W.Z., 2001. Vegetation response to the ~14.7 and ~11.5 ka cal. BP climate change: is vegetation lagging climate? Glob. Planet. Chang. 30, 103–115.
Hoek, W.Z., Bohncke, S.J.P., 2002. Climatic and environmental events over the last

termination, as recorded in The Netherlands: a review. Neth. J. Geosci.- Geol. Mijnb. 81, 123–137.
Houtgast, R.F., Van Balen, R.T., Bouwer, L.M., Brand, G.B.M., Brijker, J.M., 2002. Late quaternary activity of the Feldbiss fault zone, Roer Valley rift system, based on displaced fluvial terrace fragments. Tectonophysics 352, 295–315.
Houtgast, R.F., Van Balen, R.T., Kasse, C., Vandenberghe, J., 2003. Late quaternary tectonic evolution and postseismic near surface fault displacements along the Geleen fault (Feldbiss fault zone – Roer Valley rift system, The Netherlands), based on trenching. Neth. J. Geosci.- Geol. Mijnb. 82, 177–196.
Houtgast, R.F., Van Balen, R.T., Kasse, C., 2005. Late quaternary evolution of the Feldbiss fault (Roer Valley rift system, The Netherlands) based on trenching, and its potential relation to glacial unloading. Quat. Sci. Rev. 24, 491–510.
Jakobsson, M., Björk, S., O'Regan, M., Flodén, T., Greenwood, S., Swärd, H., Lif, A., Ampel, L., Koyi, H., Skelton, A., 2014. Major earthquake at the Pleistocene-Holocene transition in Lake Vättern, southern Sweden. Geology 42, 379–382.
Joordens, J.C.A., d'Errico, F., Wesselingh, F.P., Munro, S., De Vos, J., Wallinga, J., Ankjærgaard, C., Reimann, T., Wijbrans, J.R., Kuiper, K.F., Mücher, H.J., Coqueugniot, H., Prié, V., Joosten, I., Van Os, B., Schulp, A.S., Panuel, M., Van der Haas, V., Lustenhouwer, W., Reijmer, J.J.G., Roebroeks, W., 2014. Homo erectus from Trinil used shells for tool production and engraving. Nature. https://doi.org/10.1038/nature13962.
Kars, R.H., Busschers, F.S., Wallinga, J., 2012. Validating post IRIRSL dating on K-feldspars through comparison with quartz OSL ages. Quat. Geochronol. 12, 74–86.
Kasse, C., Vandenberghe, D., De Corte, F., Van den Haute, P., 2007. Late Weichselian fluvio-aeolian sands and coversands of the type locality Grubbenvorst (southern Netherlands): sedimentary environments, climate record and age. J. Quat. Sci. 22, 695–708.
Kasse, C., Tebbens, L.A., Trump, M., Deeben, J., Derese, C., De Grave, J., Vandenberghe, D., 2018. Late Glacial and Holocene aeolian deposition and soil formation in relation to the Late Paleolithic Ahrensburg occupation, site Geldrop-A2, The Netherlands. Neth. J. Geosci.-Geol. Mijnb. 71, 3–29.
Kiden, P., Denys, L., Johnston, P., 2002. Late Quaternary sea-level change and isostatic and tectonic land movements along the Belgian-Dutch North Sea coast: geological data and model results. J. Quat. Sci. 17, 535–546.
Kübler, S., Streich, R., Lück, E., Hoffmann, M., Friedrich, A., Strecker, M., 2017. Active faulting in a populated low-strain setting (Lower Rhine Graben, Central Europe) identified by geomorphic, geophysical and geological analysis. Geol. Soc. Lond. Spec. Publ. 432, 127–146. https://doi.org/10.1144/SP432.11.
Lowe, D.R., 1975. Water escape structures in coarse-grained sediments. Sedimentology 22, 157–204.
McCalpin, J., 1996. Paleoseismology. Academic Press, London, p. 588.
Michon, L., Van Balen, R.T., Merle, O., Pagnier, H., 2003. Cenozoic evolution of the Roer Valley rift system integrated at european scale. Tectonophysics 367, 101–126.
Michon, L., Van Balen, R.T., 2005. Characterization and quantification of active faulting in the Roer valley rift system based on high precision digital elevation models. Quat. Sci. Rev. 24, 457–474.
Mörner, N.A., 1978. Faulting, fracturing and seismic activity as a function of glacial-isostasy in Fennoscandia. Geology 6, 41–45.
Mörner, N.A., 2013. Patterns in seismology and paleoseismology, and their application on long-term hazard assessments - the Swedish case in view of nuclear waste management. Pattern Recognit. Phys. 1, 75–89.
Muir-Wood, R., 2000. Deglaciation seismotectonics: a principal influence on intraplate seismogenesis at high latitudes. Quat. Sci. Rev. 19, 1399–1411.
Murray, A.S., Wintle, A.G., 2003. The single aliquot regenerative dose protocol: potential for improvements in reliability. Radiat. Meas. 37, 377–381.
Obermeier, S.F., 1996. Use of liquefaction-induced features for paleoseismic analysis- an overview of how seismic liquefaction features can be distinguished from other features and how their regional distribution and properties of source sediment can be used to infer the location and strength of Holocene paleo-earthquakes. Eng. Geol. 44, 1–76.
Peeters, J., Busschers, F.S., Stouthamer, E., Bosch, J.H.A., Van den Berg, M.W., Wallinga, J., Versendaal, A.J., Bunnik, F.P.M., Middelkoop, H., 2016. Sedimentary architecture and chronostratigraphy of a late Quaternary incised valley fill: a case study of the late Middle and Late Pleistocene Rhine system in The Netherlands. Quat. Sci. Rev. 131, 211–236. https://doi.org/10.1016/j.quascirev.2015.10.015.
Reimer, P.J., Bard, E., Bayliss, A., Beck, J.W., Blackwell, P.G., Bronk Ramsey, C., Buck, C.E., Cheng, H., Edwards, R.L., Freidrich, M., Grootes, P.M., Guilderson, T.P., Haflidason, H., Hajdas, I., Hatte, C., Heaton, T.J., Hoffmann, D.G., Hogg, A.G., Hughen, K.A., Kaiser, K.F., Kromer, B., Manning, S.W., Nui, M., Reimer, R.W., Richards, R.A., Scott, E.M., Southon, J.R., Staff, R.A., Turney, C.M.S., Van der Plicht, J., 2013. IntCal13 and Marine13 calibration curves 0–50,000 Years BP. Radiocarbon 55 (4), 1869–1887.
Rhodes, E.J., 2011. Optically stimulated luminescence dating of sediments over the past 200,000 Years. Annu. Rev. Earth Planet. Sci. https://doi.org/10.1146/annurev-earth-040610-133425.
Sandersen, P.B., Jørgensen, F., 2014. Neotectonic deformation of a Late Weichselian outwash plan by deglacation-induced fault reactivation of a deep-seated graben structure. Boreas 44, 413–431.
Schokker, J., Koster, E.A., 2004. Sedimentology and facies distribution of Pleistocene cold climate aeolian and fluvial deposits in the Roer Valley Graben (southeastern Netherlands). Permafr. Periglac. Process. 15, 1–20.
Schokker, J., Cleveringa, P., Murray, A.S., Westerhoff, W.E., 2005. An OSL dated middle and late quaternary sedimentary record in the Roer Valley graben (southeastern Netherlands). Quat. Sci. Rev. 24, 2243–2264.
Schokker, J., Weerts, H.J.T., Westerhoff, W.E., Berendsen, H.J.A., Den Otter, C., 2007. Introduction of the Boxtel Formation and implications for the quaternary lithostratigraphy of The Netherlands. Neth. J. Geosci.– Geol. Mijnb. 86, 197–210.
Sevink, J., Koster, E.A., Van Geel, B., Wallinga, J., 2013. Drift sands, lakes, and soils: the multiphase Holocene history of the Laarder Wasmeren area near Hilversum, The Netherlands. Neth. J. Geosci./Geol. Mijnb. 92, 243–266.
Steffen, R., Wu, P., Steffen, H., Eaton, D.W., 2014. The effect of earth rheology and ice-sheet size on faults slip and magnitude of postglacial earthquakes. Earth Planet. Sci. Lett. 388, 71–80.
Thiel, C., Buylaert, J.P., A., Murray, A., Terhorst, B., Hofer, I., Tsukamoto, S., Frechen, M., 2011. Luminescence dating of the Stratzing loess profile (Austria) – testing the potential of an elevated temperature post-IR IRSL protocol. Quat. Int. 234 (1–2), 23–31. https://doi.org/10.1016/j.quaint.2010.05.018.
Van Balen, R.T., Houtgast, R.F., Cloetingh, S.A.P.L., 2005. Neotectonics of The Netherlands. Quat. Sci. Rev. 24, 439–454.
Van den Berg, M., Vanneste, K., Dost, B., Lokhorst, A., Van Eijk, M., Verbeeck, K., 2002. Paleoseismic investigations along the Peel Boundary Fault: geological setting, site selection and trenching results. Neth. J. Geosci.– Geol. Mijnb. 81, 39–60.
Van den Broek, J.M.M., Maarleveld, G.C., 1963. The Late-Pleistocene terrace deposits of the Meuse. Meded. Geol. Sticht. NS 16, 13–24.
Vandenberghe, D., Vanneste, K., Verbeeck, K., Paulissen, E., Buylaert, J.P., De Corte, F., Van den Haute, P., 2009. Late Weichselian and Holocene earthquake events along the Geleen fault in NE Belgium: OSL age constraints. Quat. Int. 199, 56–74.
Vandenberghe, J., 2006. Cryoturbation structures. In: Elias, S.A. (Ed.), Encyclopedia of Quaternary Science, pp. 2147–2153.
Vandenberghe, D.A.G., Derese, C., Kasse, C., Van den Haute, P., 2013. Late Weichselian (fluvio-) aeolian sediments and Holocene drift-sands of the classical type locality in Twente (E Netherlands): a high-resolution dating study using optically stimulated luminescence. Quat. Sci. Rev. 68, 96–113.
Van Eck, T., Davenport, C.A., 1994. Seismotectonics and seismic hazard in the Roer Valley graben; with emphasis on the Roermond earthquake of April 13, 1992. Geol. Mijnb. 73, 91–92.
Van Hoesel, A., Hoek, W.Z., Braadbaart, F., F., Van der Plicht, J., Pennock, G.M., Drury, M.R., 2012. Nanodiamonds and wildfire evidence in the Usselo horizon postdate the Allerød-Younger Dryas boundary. Proc. Natl. Acad. Sci. Unit. States Am. 109, 7648–7653.
Vanneste, K., Verbeeck, K., 2001. Paleoseismological analyses of the Rurrand fault near Jülich, Roer Valley graben, Germany: coseismic or aseismic faulting history? Neth. J. Geosci.– Geol. Mijnb. 80, 155–170.
Vanneste, K., Meghraoui, M., Camelbeeck, T., 1999. Late Quaternary earthquake-related soft-sediment deformation along the Belgian portion of the Feldbiss fault, Lower Rhine graben system. Tectonophysics 309, 57–79.
Vanneste, K., Camelbeeck, T., Verbeeck, K., Demoulin, A., 2018. Morphotectonics and past large earthquakes in eastern Belgium. In: Demoulin, A. (Ed.), Landscapes and Landforms of Belgium and Luxembourg. World Geomorphological Landscapes, pp. 215–236. https://doi.org/10.1007/978-3-319-58239-9_13.
Van Vliet Lanoë, N., Magyari, A., Meilliez, F., 2004. Distinguishing between tectonic and periglacial deformations of quaternary continental deposits in Europe. Glob. Planet. Chang. 43, 103–127.
Verbeeck, K., Wouters, L., Vanneste, K., Camelbeeck, T., Vandenberghe, D., Beerten, K., Rogiers, B., Schiltz, M., M., Burow, C., Mees, F., De Grave, J., Vandenberghe, N., 2017. Episodic activity of a dormant fault in tectonically stable Europe: the Rauw fault (NE Belgium). Tectonophyisics 699, 146–163.
Vink, A., Steffen, H., Reinhardt, L., Kaufmann, G., 2007. Holocene relative sea-level change, isostatic subsidence and the radial viscosity structure of the mantle of northwest Europe (Belgium, The Netherlands, Germany, southern north Sea). Quat. Sci. Rev. 26, 3249–3275.
Wallinga, J., Bos, I.J., 2010. Optical dating of clastic lake-fill sediments – a feasibility study in the Holocene Rhine delta (western Netherlands). Quat. Geochronol. 5, 602–610.
Wallinga, J., Murray, A.S., Wintle, A.G., 2000. The single-aliquot regenerative-dose (SAR) protocol applied to coarse-grain feldspar. Radiat. Meas. 32, 529–533.
Wallinga, J., Bos, A.J.J., Dorenbos, P., Murray, A.S., Schokker, J., 2007. A test case for anomalous fading correction in IRSL dating. Quat. Geochronol. 2, 216–221.
Wells, D.L., Coppersmith, K.J., 1994. New empirical relationships among magnitude, rupture length, rupture width, rupture area, and surface displacement. Bull. Seismol. Soc. Am. 974–1002.
Wintle, A.G., 2008. Fifty years of luminescence dating. Archaeometry 50, 276–312.
Wintle, A.G., Murray, A.S., 2006. A review of quartz optically stimulated luminescence characteristics and their relevance in single-aliquot regeneration dating protocols. Radiat. Meas. 41, 369–391.
Woolderink, H.A.G., Kasse, C., Cohen, K.M., Hoek, W.Z., Van Balen, R.T., 2018. Spatial and temporal variations in river terrace formation, preservation, and morphology in the Lower Meuse Valley, The Netherlands. Quat. Res. 1–22. https://doi.org/10.1017/qua.2018.49.
Yi, S., Buylaert, J.P., Murray, A.S., Lu, H., Thiel, C., Zeng, L., 2016. A detailed post-IR IRSL study of the Niuyangzigou loess site in northeastern China. Boreas. https://doi.org/10.1111/bor.12185.
Ziegler, P.A., 1992. European Cenozoic rift system. Tectonophysics 208, 91–111.